González Espín, FJ.; Patrao Herrero, I.; Figueres Amorós, E.; Gabriel Garcerá (2013). An Adaptive Digital Control Technique for Improved Performance of Grid Connected Inverters. IEEE Transactions on Industrial Informatics. 9(2):708-718. doi:10.1109/TII.2012.2225437.

An Adaptive Digital Control Technique for Improved Performance of Grid Connected Inverters

Fran González-Espín, *Member, IEEE*, Iván Patrao, Gabriel Garcerá, *Member*, *IEEE*, Emilio Figueres, *Senior Member, IEEE*

***Abstract*—Grid connected Voltage Source Inverters (VSI) may be controlled in the stationary reference frame (StRF) by means of the infinite impulse response (IIR) P+Resonat regulator. This regulator is able to correctly track fixed frequency sinusoidal references, but does not perform well if the frequency of the electric grid voltage is varied. In order to avoid the lack of precision to track variable frequency sinusoidal references, an adaptive IIR filter structure is proposed which offers good tracking properties even if the frequency of the grid voltage varies. This filter adapts its coefficients in real time and is inherently stable no matter the adaptation process, thus overcoming one of the most important drawbacks of the IIR filter structure. Furthermore, this structure is perfectly suited to be programmed in fixed point DSPs because of some important numeric properties, i.e. it has a high mapping precision and a low round-off accumulation, and it avoids quantization limit cycle oscillations. The proposed adaptive controller has been tested by means of the TI TMS320F2812 DSP. The obtained experimental results show up that this controller allows the correct tracking of a sinusoidal reference, even if this reference is time variant.**

***Index Terms*-- Adaptive control, converters, current control, digital control inverters, photovoltaic systems, power conversion harmonics, power quality, solar energy, three-phase electric power.**

I. NOMENCLATURE

β_v, β_i	Sensing gains of the PV output voltage and PV inverter output current.
C_f	Capacitance of the LCL filter.
$\tilde{d}$	Current disturbance small-signal.
D_α, D_β	Projection into the StRF of the duty cycle at the operating-point.
$\tilde{d}_\alpha$, $\tilde{d}_\beta$	Projection into the StRF of the duty cycle small-signal values.
θ_1, θ_2	PL controller tuning parameters in *rad*.
f_S	Sampling frequency in *Hz*.
f_{SW}	Switching frequency in *Hz*.
I_α, I_β	Projection into the StRF of the PV inverter output current at the operating-point.
I_{PV}	PV array output current at the operating-point.
$\tilde{i}_{i\alpha}$, $\tilde{i}_{i\beta}$	Projection into the StRF of the PV inverter output current small-signal values.
$\tilde{i}^*_{i\alpha}$, $\tilde{i}^*_{i\beta}$	Projection into the StRF of the reference PV inverter output current small-signal values.
$\tilde{i}_{g\alpha}$, $\tilde{i}_{g\beta}$	Projection into the StRF of the injected current small-signal values.
$\tilde{i}_{PV}$	PV array output current small-signal values.
$\tilde{i}^*_{PV}$	PV array output current reference small-signal values.
k_{PV}	PV array transconductance in *A/V*.
L_g	Grid side inductance of the LCL filter.
L_i	Inverter side inductance of the LCL filter.
R_d	Damping resistance of the LCL filter.
T_S	Sampling period in *s*.
$\tilde{v}_{c\alpha}$, $\tilde{v}_{c\beta}$	Projection into the StRF of the LCL filter capacitor (C_f) voltage small-signal.
$\tilde{v}_{g\alpha}$, $\tilde{v}_{g\beta}$	Projection into the StRF of the grid voltage small-signal values.
$\tilde{v}_{i\alpha}$, $\tilde{v}_{i\beta}$	Projection into the StRF of the PV inverter output voltage small-signal.
V_g	Grid peak voltage.
V_{PV}	PV array output voltage at the operating-point.
$\tilde{v}_{PV}$	PV array output voltage small-signal values.
$\tilde{v}^*_{PV}$	PV array output voltage reference small-signal values.
ω_{RES}	Center frequency of the P+Resonant controller in *rad/s*.
ω_{PL}	Normalized center frequency of the PL controller in *rad*.
ω_i	Grid voltage frequency in *rad/s*.
$\hat{\omega}_i$	Estimated grid voltage frequency in *rad/s*.

II. Introduction

The use of the voltage source inverter (VSI) power electronics converter to plug renewable energy sources to the electric grid, has given rise to several control techniques based on Digital Signal Processors (DSP) or Field Programmable Gate Arrays (FPGA) [1], [2]. These control techniques are able to provide a good sinusoidal reference tracking, along with a high power factor and a low injected current total harmonic distortion (THDi) [3]. One of the most interesting control techniques is implemented in the stationary reference frame (StRF), being based on the so-called P+Resonant controller, which allows a good sinusoidal reference tracking with a simple infinite impulse response (IIR) filter [4], [5]. However, this controller is designed to properly work with fixed frequency sinusoidal references, so that the performance of the VSI would be worse than that expected if the reference signal frequency were varied, e.g. an inverter operating in the islanding mode [6].

In order to obtain a controller with a good reference tracking behavior even if the grid voltage frequency varies, a filter structure with automatic frequency tuning is needed. As previously shown, the IIR structure is commonly used to implement the P+Resonant controller, mainly because its ease of implementation and its lower computational burden when compared with the equivalent FIR filter [7]. However, the IIR filter might become unstable if it is not carefully designed, especially if the coefficients of the filter have to be automatically adapted over the time. In this regard, obtaining an stable adaptive IIR filter structure has been an interesting field of research over the last years, mainly in the acoustic, speech and signal processing fields [8-11]. In addition, some adaptive filter techniques have been used in power electronics applications, although the attempts to find a suitable adaptive current controller are based on the FIR filter structure [12], while the adaptive IIR filter structure has been previously proposed as an alternative synchronization technique [13] or as a reference current generator for active filters [14]. However, the most commonly used topology to implement the adaptive filters has been the FIR structure, because of its inherently stable operation [15].

In this paper, an inherently stable adaptive controller for the VSI current control is proposed, based on the Schur-Lattice IIR filter structure [16]. This controller allows the control scheme to track the reference signal, even if its frequency varies over the time, by using the estimated phase to adapt the coefficients of the filter. The proposed controller behaves like the non-adaptive P+Resonant controller in steady-state operation, but introduces the ability to adapt its center frequency in real time, without the need of an increased filter order, as it is the case of the widely used adaptive FIR filters.

It is important to point out that the proposed IIR filter structure is inherently stable, so that the stability of the control loop is not affected by the coefficients adaptation process.

III. The Three-Phase P+Resonant Controller

The three-phase P+Resonant controller is designed to control de VSI into de StRF by means of the control structure depicted in Fig. 1. This control structure includes the photovoltaic (PV) array of panels, which output voltage is controlled by means of a Proportional+Integral (PI) controller designed in the Synchronous Reference Frame (SRF). The reference signal of this controller is obtained by a Maximum Power Point Tracking (MPPT) algorithm. Furthermore, the transfer function matrix of the current control loops shown in (1) and (2) applies [17]. In this transfer function matrix, K_{PRES} is the proportional gain, K_{RES} is the filter gain at the resonant frequency, ω_{RES}, and B_{RES} is the filter bandwidth in rad/s. This control strategy has many advantages over the synchronous reference frame (SRF) control, being the most important one the ability to carry out a naturally decoupled control of the positive and negative sequence of the inverter current [18].

$$H_{StRF}(s)=\begin{bmatrix} H_{\alpha PR}(s) & 0 \\ 0 & H_{\beta PR}(s) \end{bmatrix} \tag{1}$$

$$H_{\alpha PR}(s)=H_{\beta PR}(s)=K_{PRES}+\frac{K_{RES}B_{RES}s}{s^2+B_{RES}s+\omega_{RES}{}^2} \tag{2}$$

The Bode plot of the P+Resonant controller has been computed by means of MATLAB, obtaining the result depicted in Fig. 2, where several values of the bandwidth, B_{RES}, have been used. The center frequency, the proportional gain and the gain at the resonance frequency have been kept constant. It can be noticed that the peak gain of the controller occurs at the center frequency, and that it can be adjusted by means of the K_{RES} constant. Furthermore, the higher this gain, the more accurate is the reference tracking. However, this gain decreases abruptly at frequencies around the center frequency,

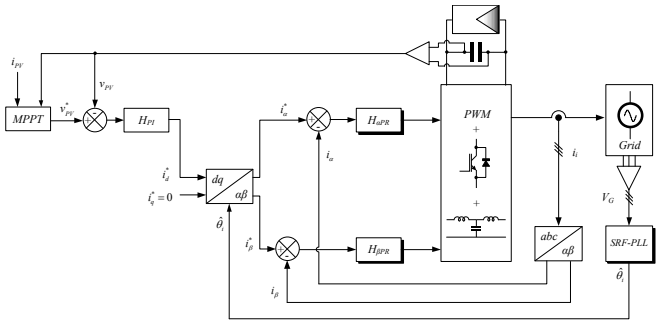

Fig. 1. Simplified schematic of the StRF control strategy.

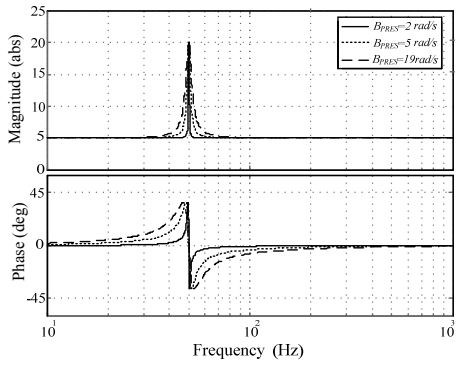

Fig. 2. Bode plot of the P+Resonant controller for $\omega_{RES}=2\pi 50 rad/s$, $K_{PRES}=5$, $K_{RES}=15$ and several B_{RES} values.

until it reaches a constant value that depends on the proportional gain, K_{PRES}. By taking into account that K_{PRES} is adjusted to assure the stability of the whole control loop, it can be affirmed that its value is usually small. In this regard, the tracking of a sinusoidal signal with a frequency other than ω_{RES} is not well accomplished by the controller.

This issue is better shown by obtaining the reference-signal-to-output-current transfer function, $G_{cl}(s)$, as well as the reference-signal-to-error transfer function, $G_e(s)$. In the Appendix of this paper has been derived the averaged small-signal linear model of the PV inverter in the StRF. By using this model, the inverter output current control loop depicted in Fig. 3 has been obtained. It should be noted that the α channel current control loop is equal to that of the β channel, so that only the study of one channel control loop is needed. The analytical expressions of the aforementioned transfer functions are shown in (3) and (4) respectively, where $T_{i\alpha}(s)$ is the open-loop gain defined by (5). Furthermore, the transfer function of the PWM modulator has been modeled by a second order Padé approximation [19] with the continuous transfer function shown in (6). The duty-cycle-to-inverter-output-current transfer function has been obtained by means of the space-state representation of the grid-connected PV inverter described in the Appendix.

$$G_{cl}(s)=\frac{\tilde{i}_\alpha}{\tilde{i}_\alpha^*}(s)=\frac{T_{i\alpha}(s)}{1+T_{i\alpha}(s)} \tag{3}$$

$$G_e(s)=\frac{\tilde{e}}{\tilde{i}_\alpha^*}(s)=\frac{1}{1+T_{i\alpha}(s)} \tag{4}$$

$$T_{i\alpha}(s)=H_{\alpha PR}(s)\cdot H_{PWM}(s)\cdot\frac{\tilde{i}_\alpha}{\tilde{d}_\alpha}(s) \tag{5}$$

$$H_{PWM}(s)=e^{-sT_d}=\frac{1-s\frac{T_d}{2}+\frac{1}{12}(sT_d)^2}{1+s\frac{T_d}{2}+\frac{1}{12}(sT_d)^2},\quad T_d=T_S \tag{6}$$

The Bode plots of (3) and (4) are shown in Fig. 4 (a) and Fig. 4 (b), respectively. These plots clearly show that the P+Resonant regulator perfectly tracks a reference with a frequency equal to that of the center frequency of the P+Resonant controller, ω_{RES}. However, if the frequency of the reference signal varies, the control loop is not able to perform the correct tracking. In order to avoid the lack of gain of the conventional P+Resonant controller, an inherently stable and numerically robust adaptive filter is proposed next. This filter is based on the Schur-lattice IIR structure, and it allows

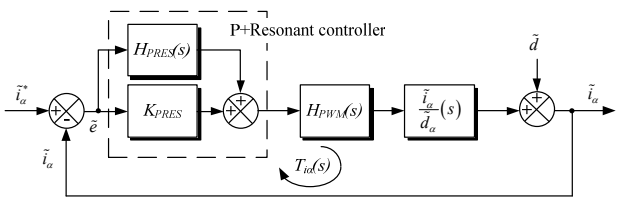

Fig. 3. Control of the $\tilde{i}_\alpha$ term by means of the P+Resonant controller.

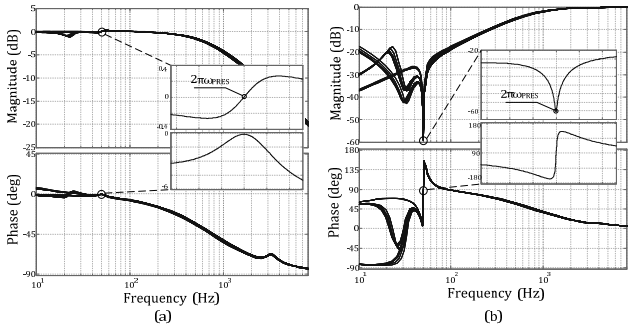

Fig. 4. Bode plot of (a) the inverter-output-current-to-reference-signal transfer function and (b) error-to-reference-signal transfer function.

obtaining an alternative resonant filter, whose coefficients can be adapted in real time. In this regard, all the poles of the filter remain inside the unit circle (i.e. the filter is causal and stable) [16].

IV. The Proposed Three-Phase Proportional+Lattice StRF Controller

A. The Adaptive Schur-lattice IIR Filter Structure

The adaptive Schur-lattice IIR filter structure is based on the block diagram depicted in Fig. 5 (a), where each of the blocks θ_k represent the Schur-lattice recursion and are described in Fig. 5 (b) [20]. Furthermore, the Schur-lattice recursion carries out the rotation over the transfer functions involving the filtering process expressed in (7). Therefore, the all-pass transfer function $\hat{F}_2(z)$ shown in (8) is obtained for the second order lattice filter depicted in Fig. 5 (a), where $H_L(z)$ is the transfer function of the band-pass resonant filter described by (9).

$$\begin{bmatrix}F_{k-1}(z)\\ \hat{F}_k(z)\end{bmatrix}=\begin{bmatrix}\cos(\theta_k) & -\sin(\theta_k)\\ \sin(\theta_k) & \cos(\theta_k)\end{bmatrix}\begin{bmatrix}F_k(z)\\ z^{-1}\hat{F}_{k-1}(z)\end{bmatrix} \tag{7}$$

$$\hat{F}_2(z)=\frac{\sin(\theta_2)+\sin(\theta_1)\left(1+\sin(\theta_2)\right)z^{-1}+z^{-2}}{1+\sin(\theta_1)\left(1+\sin(\theta_2)\right)z^{-1}+\sin(\theta_2)z^{-2}} \tag{8}$$

$$H_L(z)=\frac{K_L}{2}\cdot\left(1-\hat{F}_2(z)\right) \tag{9}$$

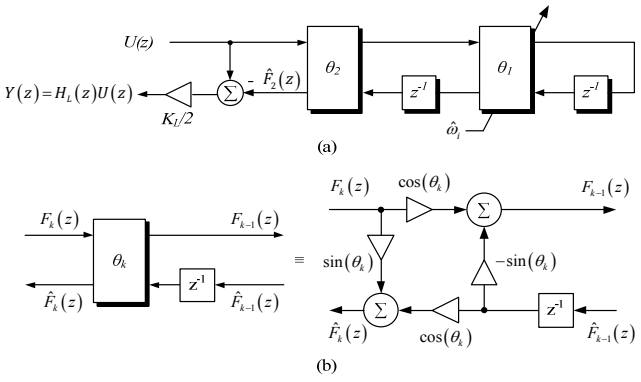

Fig. 5. Block diagram of the (a) adaptive Schur-lattice resonant filter and (b) schur-recursion.

This filter structure has many desirable properties for fixed coefficients digital filtering, which make it a good choice to implement a time-variant coefficients IIR filter by using either a fixed-point or a floating point digital signal processor [10]:

- The structure is inherently limited to realize stable and causal filters. This means that the adaptation process cannot result in an unstable filter.
- All the internal nodes are inherently scaled in the l2 sense (also known as the Euclidean norm). This property assures that the same Q-format can be used to program the filter, so that precision is not lost in the filtering process.
- Round-off noise accumulation in the state vector loop is inherently low irrespective of the poles of the filter. In this regard, the mapping of the poles and zeros is more precise no matter the position of the poles and zeros. This property is very interesting in low-frequency signals with high-frequency sampling.
- Limit cycles due to quantization can be easily suppressed.

The Schur-lattice IIR filter structure has the discrete transfer function shown in (10), which is a second order IIR filter. Therefore, the coefficients θ_1 and θ_2 can be adjusted in order to tune the center frequency, ω_{PL}, and the bandwidth, B_{PL}, of the band-pass filter, according to (11) and (12), respectively. The gain at the center frequency is adjusted by means of K_L. Fig. 6 shows the transfer function Bode plots for several θ_2 values, when θ_1 is kept constant so that the normalized center frequency remains $\omega_0=\pi/2$ *rad.*

$$H_L(z)=\frac{K_L}{2}\cdot\frac{\left(1-\sin(\theta_2)\right)\left(1-z^{-2}\right)}{1+\sin(\theta_1)\left(1+\sin(\theta_2)\right)z^{-1}+\sin(\theta_2)z^{-2}} \quad (10)$$

$$\omega_{PL}=\theta_1+\frac{\pi}{2},\qquad |\theta_1|<\frac{\pi}{2} \quad (11)$$

$$B_{PL}=-2\tan^{-1}\left(\frac{\sin(\theta_2)-1}{\sin(\theta_2)+1}\right) \quad (12)$$

In order to adapt the normalized center frequency, ω_{PL}, when the grid voltage frequency, ω_i, varies, the estimated frequency, $\hat{\omega}_i$ (obtained by the grid synchronization algorithm), can be used. It is worth pointing out that the most usual synchronization techniques used in grid connected VSI are based on a phase-locked look (PLL) algorithm, which indirectly compute the estimated phase [21]. Taking into account that the filter resonant frequency is wanted to be equal to the estimated frequency (i.e. $f_S\cdot\omega_{PL}=\hat{\omega}_i$), (13) is finally obtained by operating in (11), which allows the parameter θ_1 to be correctly tuned in real time. It should be noted that the θ_1 maximum absolute value restriction is related with the Nyquist theorem, and, as it will be further shown, it does not limit the stability of the real time adaptation process.

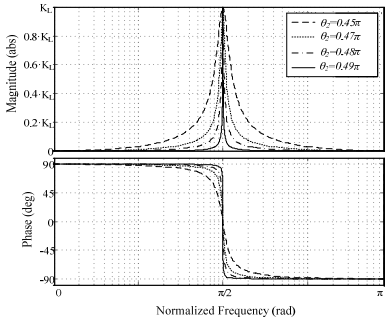

Fig. 6. Schur-lattice resonant band-pass Bode plot for several θ_2 values and for constant θ_1 (i.e. constant filter normalized resonant frequency, ω_{PL}).

$$\theta_1=\omega_{PL}-\frac{\pi}{2},\ \omega_{PL}=\frac{\hat{\omega}_i}{f_S}\ \rightarrow\ \theta_1=\frac{\hat{\omega}_i}{f_S}-\frac{\pi}{2},\ |\theta_1|<\frac{\pi}{2} \quad (13)$$

B. Stability of the Adaptive Schur-lattice IIR Structure

Due to the fact that the coefficients of the resonant IIR filter have to be adapted in real time, it is mandatory to study the relationship between the stability of the algorithm and the variation of its coefficients. This task has been previously accomplished in [22], being based on the Schur-Cohn stability test [23]. This test demonstrates that a function $f_0(z)$ is bounded real *iff* the next two conditions come true: (i) $|f_0(0)|<1$ and (ii) the function $f_1(z)$ defined by (14) is bounded real.

$$f_1(z)=z^{-1}\frac{f_0(z)-f_0(0)}{1-f_0(z)f_0(0)} \quad (14)$$

On the one hand, the function $f_1(z)$ could be tested in the same way that the function $f_0(z)$, thus obtaining the sequence of transfer functions $f_0(z), f_1(z), \cdots, f_M(z)=1$, being M the filter order. On the other hand, the sequence of numbers $f_0(0), f_1(0), \cdots, f_{M-1}(0)$, called the Schur parameters, are used to test the stability of $f_0(z)$, by means of the Schur-Cohn stability test. This test establishes that $f_0(z)$ is bounded real *iff* all the Schur parameters are smaller than one.

This test could be applied to the transfer function $f_0(z)=\hat{F}_M(z)$ in order to find the stability condition, where M is the order of the lattice filter. By equating (7) in (14), and by studying the obtained transfer function for $k=2$ (i.e. the filter order), (15) yields, which shows up that $\sin(\theta_2)=f_0(0)$ is the first Schur parameter. Furthermore, a straightforward recursive operation over (15) gives (16), so that according to the Schur-Cohn stability test, the presented second order Schur-lattice resonant band-pass filter will be stable *iff* (17) holds.

$$f_1(z)=z^{-1}\frac{\hat{F}_2(z)-\sin(\theta_2)}{1-\hat{F}_2(z)\cdot\sin(\theta_2)} \quad (15)$$

$$f_k(0)=\sin(\theta_{M-k}),\quad k=0,\ 1,\ \ldots,\ M-1 \quad (16)$$

$$|\sin(\theta_{M-k})|<1,\quad k=0,\ 1,\ \ldots,\ M-1 \quad (17)$$

It is important to point out that (17) is always true when the Schur-lattice structure is used to implement the IIR filter, except for the angles $\theta_{M-k}=\pm\pi/2$, $k=0,\ 1,\ ...,\ M-1$. However, if this condition arises, then the all-pass function

$\hat{F}_2(z) \equiv 1$, as the zeros and the poles are located at the unit circle and consequently they cancel out; moreover, the Schur recursion makes these reciprocal roots to cancel out at the output of the filter because of the same reason [10], so that the stability can be still assured even if this condition arises.

Taking into account that the parameters of the filter have to be adapted in real time, it should be noted that the conclusion about stability derived above is of a great interest, since the use of the Schur-lattice IIR structure proposed in Fig. 5, provides an inherently stable IIR filter regardless of the filter coefficients adaptation process.

C. The Proposed Proportional+Lattice (PL) StRF Controller

Fig. 7 (a) shows the proposed Proportional+Lattice (PL) regulator block diagram, where five adaptive Schur-lattice controllers are used in parallel with a proportional controller. As it will be shown in the next chapter, this allows a better disturbance rejection of the most usual voltage harmonics (i.e. 5th, 7th, 11th and 13th), no matter the grid voltage frequency. It should be noted that each of the lattice controllers, $H_{Ln}(z)$, includes the estimated frequency, $n\hat{\omega}_i$, as an input, where $n = \{1, 5, 7, 11, 13\}$. The transfer function of the PL controller is shown in (18), whose Bode plots are depicted in Fig. 7 (b) for fixed θ_{1n}, K_{Ln} and K_{PL}, when the input frequency is 50Hz and 55Hz. Eq. (13) is used to adjust θ_{2n} in real time.

$$H_{PL}(z) = K_{PL} + \sum_n \frac{K_{Ln}/2\,(1-\sin(\theta_{2n}))(1-z^{-2})}{1+\sin(\theta_{1n})(1+\sin(\theta_{2n}))z^{-1}+\sin(\theta_{2n})z^{-2}} \tag{18}$$

V. Control of the Three Phase Inverter in the StRF by means of the PL Controller

The proposed control strategy is depicted in Fig. 8, where the conventional P+Resonant controller has been replaced by proposed PL controller depicted in Fig. 7 (a). Moreover, the synchronization method must provide the estimated frequency of the grid voltage, $\hat{\omega}_i$. It is important to point out that the estimated frequency must have a negligible ripple to avoid the PL to start swinging. Hence, the estimated frequency has been processed by means of a second order low-pass filter in order to avoid this problem.

The open loop gain of each of the control loops shown in Fig. 9 has been studied. The transfer functions are described in (19), (20) and (21), where the small-signal transfer functions $\tilde{v}_{PV}/\tilde{i}_\alpha(z)$, $\tilde{i}_\alpha/\tilde{d}_\alpha(z)$, $\tilde{i}_\beta/\tilde{d}_\beta(z)$ are the discretized transfer functions of the grid-connected PV inverter described

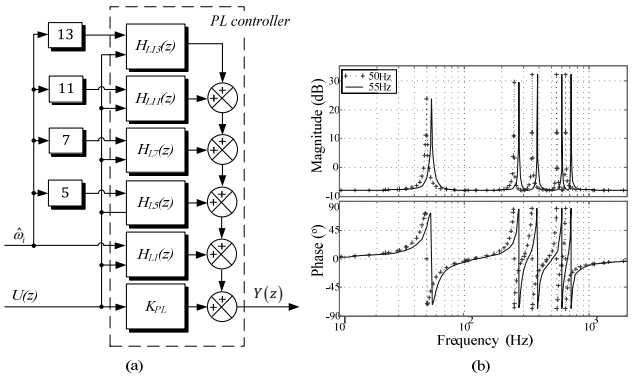

Fig. 7. Proposed PL regulator (a) block diagram and (b) Bode plots for constant values of K_{PL}, K_L and θ_2.

in the Appendix of this paper. The Proportional+Integral (PI) controller, $H_{PI}(z)$, is defined in (22), where K_P is the proportional constant and K_I is the integral constant.

$$T_V^{PL}(z) = H_{PI}(z)\cdot\beta_v/\beta_i \cdot \frac{\tilde{v}_{PV}}{\tilde{i}_\alpha}(z)\cdot H_{LP}(z) \tag{19}$$

$$T_{i\alpha}^{PL}(z) = H_{PL}(z)\cdot H_{PWM}(z)\cdot\frac{\tilde{i}_\alpha}{\tilde{d}_\alpha}(z)\cdot\beta_i\cdot H_{AA}(z) \tag{20}$$

$$T_{i\beta}^{PL}(z) = H_{PL}(z)\cdot H_{PWM}(z)\cdot\frac{\tilde{i}_\beta}{\tilde{d}_\beta}(z)\cdot\beta_i\cdot H_{AA}(z) \tag{21}$$

$$H_{PI}(z) = K_P\left(1 + K_i\frac{T_S}{2}\cdot\frac{(1+z^{-1})}{(1-z^{-1})}\right) \tag{22}$$

It should be noted that the sensing gains β_v and β_i, as well as the transfer functions of the anti-aliasing filter and the second order low-pass filter, $H_{AA}(z)$ and $H_{LP}(z)$, respectively, have been included in order to achieve a more accurate Bode plots. It is worth pointing out that $H_{LP}(z)$ is designed to attenuate the low-frequency harmonics that will appear at the

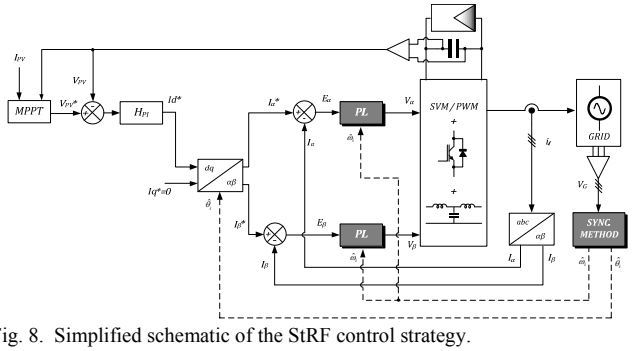

Fig. 8. Simplified schematic of the StRF control strategy.

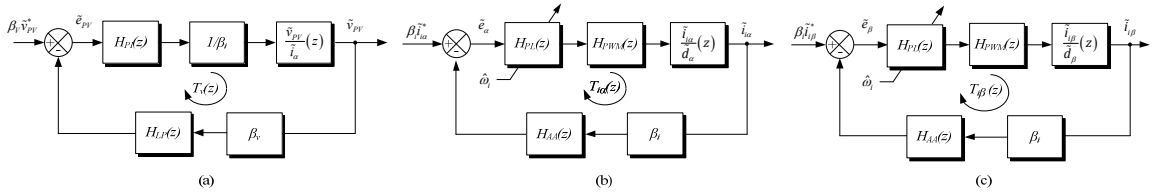

Fig. 9. Block diagram of the discretized (a) PV array output voltage control, (b) α channel current control and (c) β channel current control.

DC-link if some voltage unbalance is present at the grid. The Bode plots are used to carry out the control loops controllers design, so that the PI controller, $H_{PI}(z)$, and the PL controller, $H_{PL}(z)$, are properly tuned.

By taking into account the averaged small-signal model derived in the Appendix, the most important parameters of the 10kW PV inverter shown in Table I have been considered. Moreover, the operating point values are shown in Table II. It is important to point out that a set of PV array maximum power point (MPP) voltage, MPP current and transconductance (i.e. $V_{PV}(MPP)$, $I_{PV}(MPP)$, $k_{PV}(MPP)$ respectively) have been chosen. This allows taking into account the expected irradiance variation. Furthermore, since the operation point of the inverter StRF small-signal model depends on the phase of the grid voltage, θ_i, several values for this parameter have been considered.

Once the important parameters of the converter have been chosen, the tuning of the controllers parameters has been carried out by means of the frequency domain loop-shaping techniques.

The obtained controllers' parameters are shown in Table III and the Bode plots of the open-loop gains $T_V^{PL}(z)$ and $T_{i\alpha}^{PL}(z)$ are depicted in Fig. 10 (a) and Fig. 10 (b), respectively, for a grid frequency $\omega_i=2\pi 50 rad/s$. The stability of the system has been tested at 40Hz and at 60Hz too. The obtained results are shown in Table IV, where it is clearly stated that the inverter is stable in the entire range of frequency variation considered (i.e. 40Hz~60Hz).

In order to test the performance of the PL controller, the Bode plots of both the reference-signal-to-inverter-output-current transfer function, $G_{cl}^{PL}(z)$, and the reference-signal-to-error transfer function, $G_e^{PL}(z)$, have been obtained for several values of the grid voltage frequency (i.e. $\omega_i = \{2\pi 40,\ 2\pi 50,\ 2\pi 60\}$ rad/s). These two transfer functions are defined in (23) and (24), and their Bode plots are depicted in Fig. 11 (a) and Fig. 11 (b) respectively. The results shown in the previous figures highlight that the use of the inherently stable and numerically robust PL controller allows obtaining a good reference tracking no matter the frequency of the grid voltage.

TABLE I
PARAMETERS OF THE PV INVERTER

Parameter	*Value*
C_{PV}	2.04mF
β_V	$2\cdot10^{-3}$
β_i	$31\cdot10^{-3}$
f_{SW}	8000 Hz
f_S	16000 Hz
T_S	$6.25\cdot10^{-5}$ s
L_g	86 µH
R_g	36.7 mH
L_i	1.6 mH
R_i	16 mΩ
C_f	30 µF
R_d	0.5 Ω

TABLE II
OPERATING POINT VALUES OF THE PV INVERTER

Parameter	*Value*
$V_{PV(MPP)}$	[598 621 644 644 654] V
$I_{PV(MPP)}$	[3 6 9 12 15] A
$k_{PV(MPP)}$	$-10^{-3}\cdot$[5 10 14 19 23] A/V
V_g	$\sqrt{(2/3)}\cdot230$ V

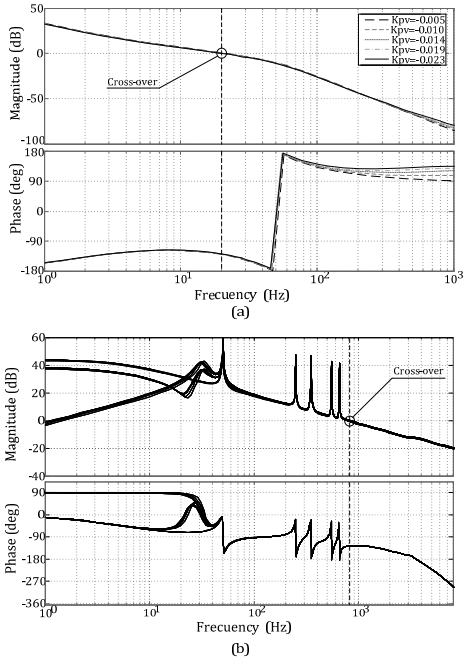

Fig. 10. Open-loop gain of the (a) PV voltage control loop and (b) α channel current control loop.

θ_i [0 π/4 π/2 3π/4 π 5π/4 3π/2 7π/4 2π] rad

TABLE III
PARAMETERS OF THE CONTROLLERS

Parameter	*Value*
K_P	-11.14
K_I	12.57
K_{PL}	0.42
K_{L1}	15
K_{L5}	30
$K_{L7}= K_{L11}= K_{L13}$	40
$\theta_{11}(nominal)$	-0.49375π rad
$\theta_{15}(nominal)$	-0.46875π rad
$\theta_{17}(nominal)$	-0.45625π rad
$\theta_{111}(nominal)$	-0.43125π rad
$\theta_{113}(nominal)$	-0.41875π rad
$\theta_{21}= \theta_{25}= \theta_{27}= \theta_{211}= \theta_{213}$	0.495π rad

TABLE IV
STABILITY CRITERIA

Parameter	*Value*		
	40Hz	*50Hz*	*60Hz*
$T_{i\alpha}(z)$ *PM-*f_c	63.6 - 807 Hz	62.5º - 809 Hz	57.6º - 821 Hz
$T_{i\alpha}$ *(z) GM-f*	12.2dB - 3580 Hz	12.2dB - 3580 Hz	12.2dB - 3580 Hz
$T_V(z)$ *PM-*f_c		52.4º - 19.8Hz	
$T_V(z)$ *GM-f*		11.5dB - 51.5Hz	

$$G_{cl}^{PL}(z)=\frac{\tilde{i}_\alpha}{\tilde{i}_\alpha^*}(z)=\frac{1}{H_{AA}(z)}\frac{T_{i\alpha}^{PL}(z)}{1+T_{i\alpha}^{PL}(z)} \quad (23)$$

$$G_{e}^{PL}(z)=\frac{\tilde{e}_\alpha}{\tilde{i}_\alpha^*}(z)=\beta_i\cdot H_{AA}\cdot\left(\frac{1}{1+T_{i\alpha}^{PL}(z)}\right) \quad (24)$$

VI. Experimental Results

The proposed controller has been experimentally tested by means of a set-up composed of a commercial three-phase 20KW inverter (SEMIKRON SKS 35F B6U+E1CIF+B6CI 21 V12) controlled by means of a fixed point DSP (TEXAS INSTRUMENTS TMS320F2812), a 40kW DC power supply capable of emulating a PV array I-V curve (AMREL SPS-800-54-D013), a 20kVA three-phase DY isolation transformer, and the LCL filter described by Table I. The inverter has been configured so that the maximum power is extracted from the PV panel (i.e. V_{PV}=*654V* and I_{PV}=*15A*).

First of all, the open-loop frequency response of the PL controller has been measured by means of the frequency response analyzer NF FRA5097 [24]. The obtained results are shown in Fig. 12, where it can be noticed the adaptive behavior of the PL controller.

In order to test the behavior of the proposed PL controller

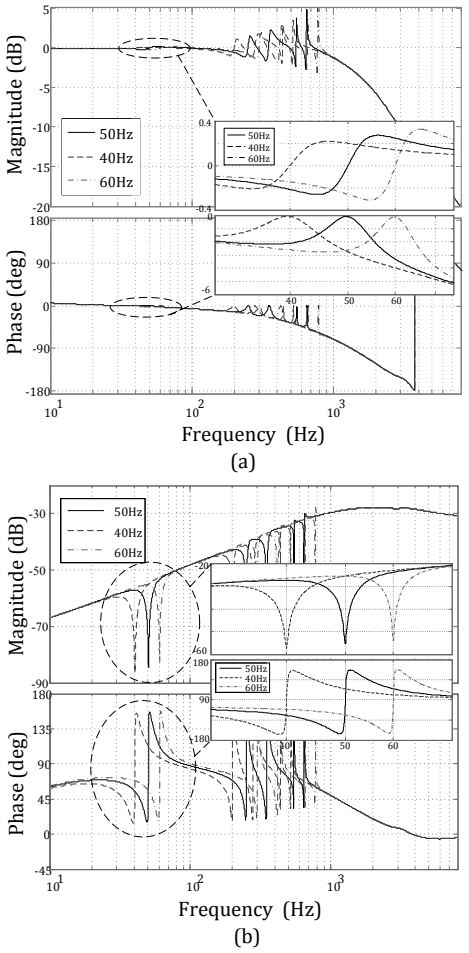

Fig. 11. Bode plot of (a) the inverter-output-current-to-reference-signal transfer function and (b) error-to-reference-signal transfer function.

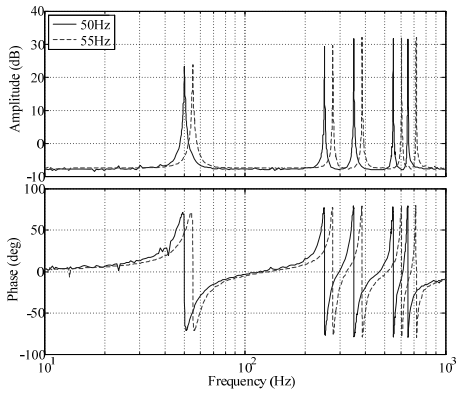

Fig. 12. Bode plot of the open-loop gain of the PL controller for a frequency of 50Hz (solid) and of 55Hz (dotted).

against the conventional P+Resonant controller, the phase-to-phase voltages in the inverter side along with the current of one phase have been measured by means of an AGILENT DSOX2004A oscilloscope, when the frequency is 40Hz, 50Hz and 55Hz. Furthermore, the total harmonic distortion of the voltage (THDv) at the inverter side is 11.5%.

The obtained results are shown in Fig. 13, where the first row belongs to the P+Resonant controller and the second row belongs to the PL controller. As it is clearly shown in Fig. 13 (a) and Fig. 13 (c), the P+Resonant controller does not perform well when the frequency is other than the fundamental (i.e. 50Hz). However, the PL controller can cope with the variation of the grid voltage frequency, as it is clearly depicted in Fig. 13 (d) and Fig. 13 (f). Furthermore, the performance of both controllers is good at the nominal frequency, as it is shown in Fig. 13 (b) and Fig. 13 (e). It should be noted that the 30^o phase shift between the measured current and voltage waveforms is due to the fact that the phase-to-phase voltage along with the line current are measured.

The THDi and the power factor (PF) have been measured by means of the electric power analyzer VOLTECH PM6000, when the grid frequency varies over the considered range (40Hz~60Hz).

In Fig. 14 (a) and Fig. 14 (b) are depicted the PF and the THDi versus the grid frequency respectively, when the conventional P+Resonant controller tuned at the nominal grid frequency (i.e. 50Hz) is used. As expected, it is clearly shown that the maximum PF and the minimum THDi are obtained when the grid frequency is the nominal one. On the contrary, the P+Resonant controller does not perform well if the grid frequency varies. In this regard, it is important to notice that a variation of +1% in the grid voltage frequency results in a THDi higher than 5%, which is beyond the most usual norms IEEE1547 and UNE-EN61000-3-2.

In Fig. 15 (a) and Fig. 15 (b) the PF and the THDi versus the grid frequency, respectively, are depicted when the proposed PL controller is used. In the plots it is clearly shown the benefits of using the inherently and numerically robust adaptive PL controller. Indeed, the PF remains constant and higher than 0.99, and the THDi is lower than 3% all over the range of grid voltage frequency variation considered, so that

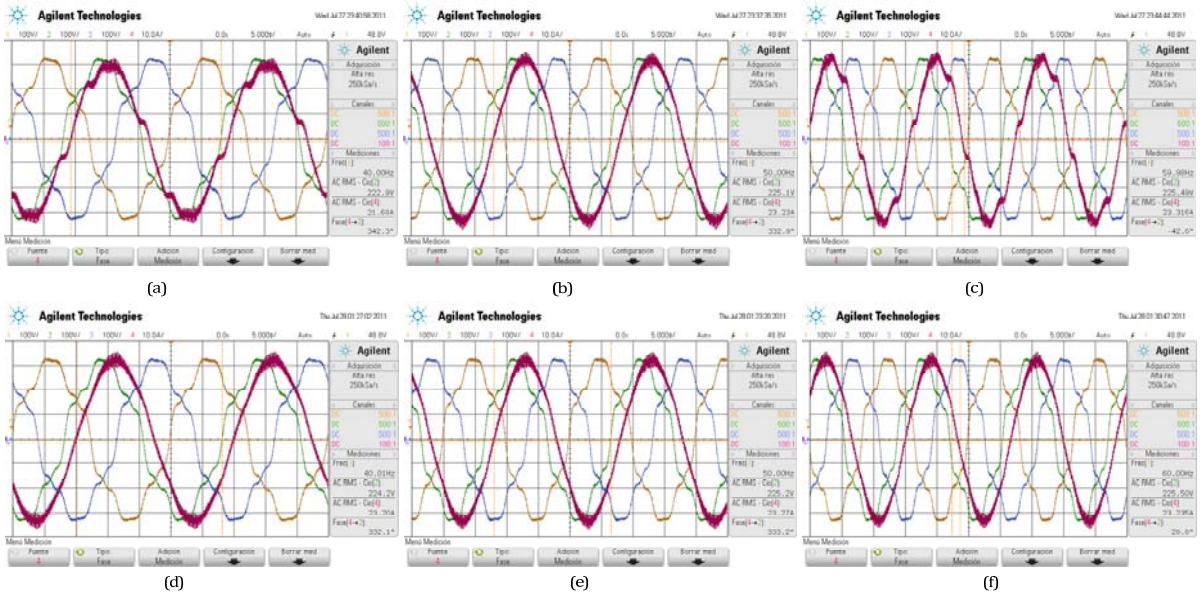

Fig. 13. Time response in steady state of the controlled current (magenta) with a THDv=11.5% and (a) P+Resonant controller (f=40Hz), (b) P+Resonant controller (f=50Hz), (c) P+Resonant controller (f=60Hz), (d) PL controller (f=40Hz), (e) PL controller (f=50Hz) and (f) PL controller (f=60Hz).

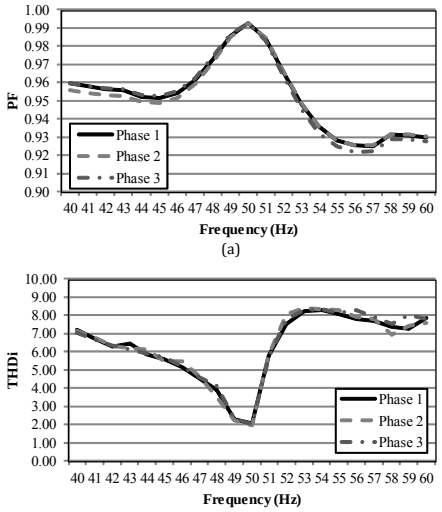

Fig. 14. Measurement of (a) PF and (b) THDi, when the grid voltage frequency is varied from 40Hz to 60Hz. P+Resonant controller.

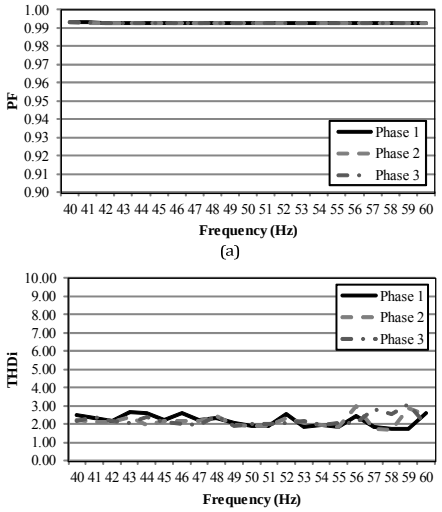

Fig. 15. Measurement of (a) PF and (b) THDi, when the grid voltage frequency is varied from 40Hz to 60Hz. PL controller.

the requirements in the aforementioned norms are met.

In order to test the stability of the PL controller, the frequency of the grid voltage has been abruptly varied from 50Hz to 55Hz. The time response of the line current along with the phase-to-phase voltages are depicted in Fig. 16. The experimental results show that the controller is stable, and that the adaptation process is almost finished in two grid cycles. In Fig. 17 a different zoom has been chosen, so that the settling time is better shown.

Finally, the computational time has been measured when using the P+Resonant and the PL controllers. The obtained results are shown in Table V.

TABLE V
COMPUTATIONAL TIME

Controller	*Time*
P+Resonant	1.5 µs
PL	7.2µs

VII. CONCLUSIONS

In this paper, a new StRF controller for grid-connected three-phase VSI based on the lattice structure has been proposed. The controller is able to track the fundamental harmonic of the grid voltage while rejecting the undesired harmonics no matter their frequency, so that a variation of the fundamental harmonic frequency does deteriorate neither the THDi nor the PF. The proposed PL can be considered more robust than the conventional P+Resonant controller due to the well-known numeric properties of the lattice structure, its ability to automatically adapt the tune frequency and its stability properties.

The experimental results obtained on a 10kW photovoltaic

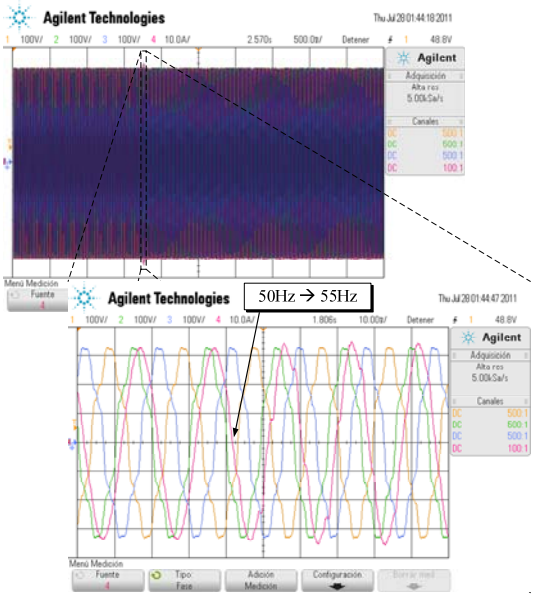

Fig. 16. Time response of the PL current controller when the frequency is abruptly varied from 50Hz to 55Hz.

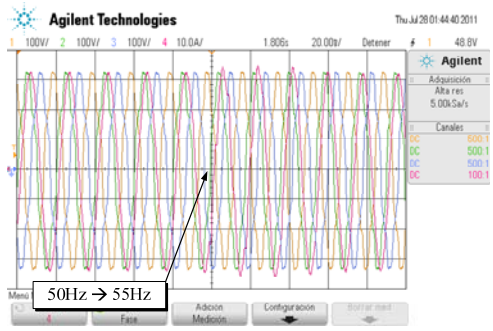

Fig. 17. Detail of the time response of the PL current controller when the frequency is abruptly varied from 50Hz to 55Hz.

inverter have shown the poor behavior of conventional P+Resonant controllers when the frequency of the grid voltage varies. On the contrary, the PL is able to maintain a constant PF near unity, and a constant THDi lower than 3% when the frequency varies from 40Hz to 60Hz.

Although the computational time of the PL is higher than the conventional P+Resonant controller, the proposed controller has many desirable properties which make it a convenient choice when using a popular fixed point digital signal processor.

APPENDIX

In order to apply the proposed adaptive linear control technique, a PV inverter StRF linear model has to be obtained [25], [26]. In Fig. 18 it is depicted the three phase PV inverter, where the inductance Li is used along with the capacitor Cf and the leakage inductance of the isolation transformer to form an LCL third order low-pass filter. The resistance Rd is chosen to add damping at the resonance frequency [27]. By operating in Fig. 18, it is possible to obtain the averaged small-signal linear model of the PV inverter depicted in Fig. 19, whose space state model is represented by (25), (26), (27), (28), (29) and (30). The operating point expressions are described in Table VI, where $L_g=L_T+L_{grid}$ and $R_g=R_T+R_{grid}$. L_T and R_T are the leakage inductance and the parasitic resistance of the isolation transformer, respectively, and L_{grid} and R_{grid} are the inductance and the resistance of the PCC connection wire.

$$\begin{aligned}\dot{\vec{x}} &= A\cdot\vec{x}+B\cdot\vec{u}\\ \vec{y} &= C\cdot\vec{x}+D\cdot\vec{u}\end{aligned} \tag{25}$$

$$A=\begin{bmatrix}
-\left(\frac{R_i+R_d}{L_i}\right) & 0 & \frac{R_d}{L_i} & 0 & -\frac{1}{L_i} & 0 & \frac{D_\alpha}{L_i}\\
0 & -\left(\frac{R_i+R_d}{L_i}\right) & 0 & \frac{R_d}{L_i} & 0 & -\frac{1}{L_i} & \frac{D_\beta}{L_i}\\
\frac{R_d}{L_g} & 0 & -\left(\frac{R_g+R_d}{L_g}\right) & 0 & \frac{1}{L_g} & 0 & 0\\
0 & \frac{R_d}{L_g} & 0 & -\left(\frac{R_g+R_d}{L_g}\right) & 0 & \frac{1}{L_g} & 0\\
\frac{1}{C_f} & 0 & -\frac{1}{C_f} & 0 & 0 & 0 & 0\\
0 & \frac{1}{C_f} & 0 & -\frac{1}{C_f} & 0 & 0 & 0\\
-\frac{D_\alpha}{C_{PV}} & -\frac{D_\beta}{C_{PV}} & 0 & 0 & 0 & 0 & \frac{k_{PV}}{C_{PV}}
\end{bmatrix} \tag{26}$$

$$B=\begin{bmatrix}
V_{PV}/L_i & 0 & 0 & 0\\
0 & V_{PV}/L_i & 0 & 0\\
0 & 0 & -1/L_g & 0\\
0 & 0 & 0 & -1/L_g\\
0 & 0 & 0 & 0\\
0 & 0 & 0 & 0\\
-I_\alpha/C_{PV} & -I_\beta/C_{PV} & 0 & 0
\end{bmatrix} \tag{27}$$

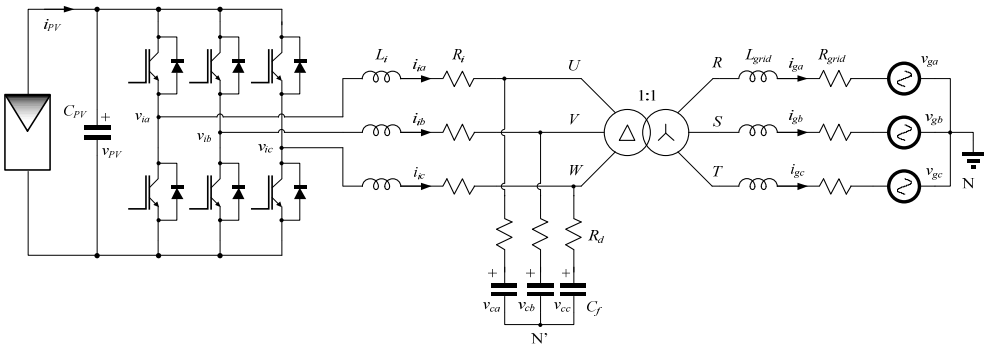

Fig. 18. PV grid connected VSI along with the LCL filter and the Δ/Y isolation transformer.

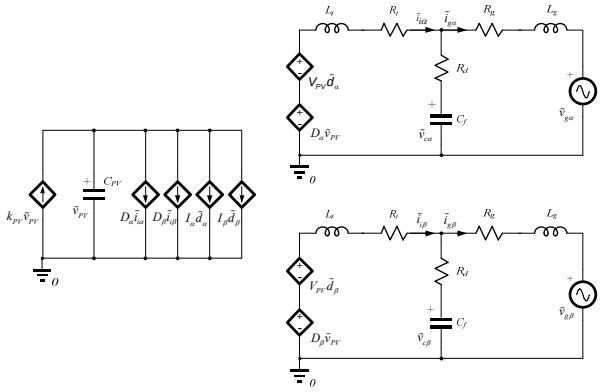

Fig. 19. Averaged small-signal linear model of the PV inverter in the StRF.

TABLE VI
EXPRESSIONS OF THE OPERATING POINT VALUES

Parameter	*Value*
D_α	$\sqrt{\frac{3}{2}}\frac{V_g}{V_{PV(MPP)}}\cos(\theta_i)$
D_β	$\sqrt{\frac{3}{2}}\frac{V_g}{V_{PV(MPP)}}\sin(\theta_i)$
I_α	$\sqrt{\frac{2}{3}}\frac{V_{PV(MPP)}I_{PV(MPP)}}{V_g}\cos(\theta_i)$
I_β	$\sqrt{\frac{2}{3}}\frac{V_{PV(MPP)}I_{PV(MPP)}}{V_g}\sin(\theta_i)$
$k_{PV(MPP)}$	$-\frac{I_{PV(MPP)}}{V_{PV(MPP)}}$

$$C = I, \quad D = 0 \tag{28}$$

$$\vec{x} = \vec{y} = \begin{bmatrix} \tilde{i}_{i\alpha} & \tilde{i}_{i\beta} & \tilde{i}_{g\alpha} & \tilde{i}_{g\beta} & \tilde{v}_{c\alpha} & \tilde{v}_{c\beta} & \tilde{v}_{PV} \end{bmatrix}^T \tag{29}$$

$$\vec{u} = \begin{bmatrix} \tilde{d}_\alpha & \tilde{d}_\beta & \tilde{v}_{g\alpha} & \tilde{v}_{g\beta} \end{bmatrix} \tag{30}$$

REFERENCES

[1] M. P. Kazmierkowski, M. Jasinski, and G. Wrona, "DSP-Based Control of Grid-Connected Power Converters Operating Under Grid Distortions," *IEEE transactions on Industrial Informatics*, vol. 7, no. 2, May2011, pp. 204-211.

[2] E. Monmasson, L. Idkhajine, M. N. Cirstea, I. Bahri, A. Tisan, and M. W. Naouar, "FPGAs in Industrial Control Applications," *IEEE transactions on Industrial Informatics*, vol. 7, no. 2, May2011, pp. 224-243.

[3] F. Blaabjerg, R. Teodorescu, M. Liserre, and A. V. Timbus, "Overview of Control and Grid Synchronization for Distributed Power Generation Systems," *IEEE Transaction on Industrial Electronics*, vol. 53, no. 5, 2006, pp. 1398-1409.

[4] D. N. Zmood and D. G. Holmes, "Stationary frame current regulation of PWM inverters with zero steady-state error," *IEEE transactions on Power Electronics*, vol. 18, no. 3, 2003, pp. 814-822.

[5] D. G. Holmes, T. A. Lipo, B. P. McGrath, and W. Y. Kong, "Optimized Design of Stationary Frame Three Phase AC Current Regulators," *IEEE transactions on Power Electronics*, vol. 24, no. 11, 2009, pp. 2417-2426.

[6] I. J. Balaguer, L. Qin, Y. Shuitao, U. Supatti, and Z. P. Fang, "Control for Grid-Connected and Intentional Islanding Operations of Distributed Power Generation," *IEEE Transaction on Industrial Electronics*, vol. 58, no. 1, Jan.2011, pp. 147-157.

[7] J. Luukko and K. Rauma, "Open-Loop Adaptive Filter for Power Electronics Applications," *IEEE Transaction on Industrial Electronics*, vol. 55, no. 2, 2008, pp. 910-917.

[8] J. E. Cousseau, S. Werner, and P. D. Donate, "Factorized All-Pass Based IIR Adaptive Notch Filters," *IEEE Transactions on Signal Processing*, vol. 55, no. 11, 2007, pp. 5225-5236.

[9] K. J. Aström and B. Wittenmark, *Adaptive Control*, 2nd ed , 2008.

[10] P. A. Regalia, *Adaptive IIR filtering in signal processing and control*. Marcel Dekker, INC., 1995.

[11] A. Nehorai, "A minimal parameter adaptive notch filter with constrained poles and zeros," *IEEE Transactions on Acoustics, Speech and Signal Processing*, vol. 33, no. 4, 1985, pp. 983-996.

[12] V. Blasko, "A Novel Method for Selective Harmonic Elimination in Power Electronic Equipment," *IEEE transactions on Power Electronics*, vol. 22, no. 1, 2007, pp. 223-228.

[13] H. A. Rivas and J. Bergas, "Frequency Determination in a Single-Phase Voltage Signal using Adaptative Notch Filters," *9th International Conference on Electrical Power Quality and Utilisation (EPQU 2007)* 2007, pp. 1-7.

[14] M. Tarek, S. Mekhilef, and N. A. Rahim, "Application of adaptive notch filter for harmonics currents estimation," *International Power Engineering Conference (IPEC 2007)* 2007, pp. 1236-1240.

[15] B. Singh and J. Solanki, "An Implementation of an Adaptive Control Algorithm for a Three-Phase Shunt Active Filter," *IEEE Transactions on Industrial Electronics*, vol. 56, no. 8, Aug.2009, pp. 2811-2820.

[16] P. A. Regalia, "Stable and efficient lattice algorithms for adaptive IIR filtering," *IEEE Transactions on Signal Processing*, vol. 40, no. 2, 1992, pp. 375-388.

[17] M. Castilla, J. Miret, J. Matas, L. Garcia de Vicuna, and J. M. Guerrero, "Control Design Guidelines for Single-Phase Grid-Connected Photovoltaic Inverters With Damped Resonant Harmonic Compensators," *IEEE Transactions on Industrial Electronics*, vol. 56, no. 11, 2009, pp. 4492-4501.

[18] D. N. Zmood, D. G. Holmes, and G. H. Bode, "Frequency-domain analysis of three-phase linear current regulators," *IEEE transactions on Industry Applications*, vol. 37, no. 2, 2001, pp. 601-610.

[19] D. M. Van de Sype, K. De Gusseme, A. P. Van den Bossche, and J. A. Melkebeek, "Small-signal Laplace-domain analysis of uniformly-sampled pulse-width modulators," *2004 Power Electronics Specialists Conference (PESC '04)* 2004, pp. 4292-4298.

[20] P. A. Regalia, S. K. Mitra, and P. P. Vaidyanathan, "The digital all-pass filter: a versatile signal processing building block," *Proceedings of the IEEE*, vol. 76, no. 1, 1988, pp. 19-37.

[21] C. Se-Kyo, "A phase tracking system for three phase utility interface inverters," *IEEE transactions on Power Electronics*, vol. 15, no. 3, 2000, pp. 431-438.

[22] A. Gray, Jr. and J. Markel, "A normalized digital filter structure," *IEEE Transactions on Acoustics, Speech and Signal Processing*, vol. 23, no. 3, June1975, pp. 268-277.

[23] P. P. Vaidyanathan and S. K. Mitra, "A unified structural interpretation of some well-known stability-test procedures for linear systems," *Proceedings of the IEEE*, vol. 75, no. 4, Apr.1987, pp. 478-497.

[24] F. Gonzalez-Espin, E. Figueres, G. Garcera, R. Gonzalez-Medina, and M. Pascual, "Measurement of the Loop Gain Frequency Response of Digitally Controlled Power Converters," *Industrial Electronics, IEEE Transactions on*, vol. 57, no. 8, Aug.2010, pp. 2785-2796.

[25] S. R. Sanders and G. C. Verghese, "Synthesis of averaged circuit models for switched power converters," *Circuits and Systems, IEEE Transactions on*, vol. 38, no. 8, 1991, pp. 905-915.

[26] H. Jiabing and H. Yikang, "Modeling and Control of Grid-Connected Voltage-Sourced Converters Under Generalized Unbalanced Operation Conditions," *Energy Conversion, IEEE Transaction on*, vol. 23, no. 3, 2008, pp. 903-913.

[27] M. Liserre, F. Blaabjerg, and S. Hansen, "Design and control of an LCL-filter-based three-phase active rectifier," *Industry Applications, IEEE Transactions on*, vol. 41, no. 5, 2005, pp. 1281-1291.